RFlens: Metasurface-Enabled Beamforming for IoT Communication and Sensing

Chao Feng*[†‡], Xinyi Li*[†‡], Yangfan Zhang[†], Xiaojing Wang[†],
Liqiong Chang[†], Fuwei Wang[†‡], Xinyu Zhang[♯], Xiaojiang Chen[†‡]

[†]Northwest University, China [♯]University of California San Diego, USA
[‡]Shaanxi International Joint Research Centre for the Battery-Free Internet of Things, China
[†]{chaofeng,xinyili,zhangyangfan1,wxj}@stumail.nwu.edu.cn, [†]{clq,wfw,xjchen}@nwu.edu.cn, [♯]xyzhang@ucsd.edu

ABSTRACT

Beamforming can improve the communication and sensing capabilities for a wide range of IoT applications. However, most existing IoT devices cannot perform beamforming due to form factor, energy, and cost constraints. This paper presents RFlens, a reconfigurable metasurface that empowers low-profile IoT devices with beamforming capabilities. The metasurface consists of many unit-cells, each acting as a phase shifter for signals going through it. By encoding the phase shifting values, RFlens can manipulate electromagnetic waves to "reshape" and resteer the beam pattern. We prototype RFlens for 5 GHz Wi-Fi signals. Extensive experiments demonstrate that RFlens can achieve a 4.6 dB median signal strength improvement (up to 9.3 dB) even with a relatively small 16×16 array of unit-cells. In addition, RFlens can effectively improve the secrecy capacity of IoT links and enable passive NLoS wireless sensing applications.

CCS CONCEPTS

• **Hardware** → **Wireless devices**; • **Networks** → **Physical links**.

KEYWORDS

Metasurface, Smart Surface, Beamforming, Wi-Fi Devices, Intelligent Transmission Surface

1 INTRODUCTION

Beamforming, or spatial filtering, represents a fundamental primitive that can enhance the wireless communication and sensing

---

*Co-primary authors, both authors contributed equally to this research.
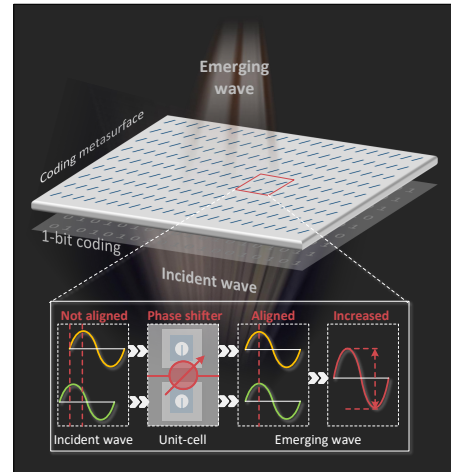

Figure 1: Basic principle of RFlens. The PIN diode determines the state of each unit-cell as 0 or 1. It can be used to synthesize arbitrary beam directions by applying specific coding sequences to the unit-cells.

capabilities in modern IoT applications. With a large array of antennas, a beamforming transmitter can focus the signal power towards the intended receiver, effectively improving the link capacity and hence reducing energy per bit [41], much desired for battery powered sensors such as surveillance cameras [1]. Also, it can use the multi-beam to enable many new applications such as multi-user wireless VR for education and gaming, where high bandwidth data must be streamed to each user. Directional beams can also reduce the risk of eavesdropping, thus improving the secrecy capacity [40]. In passive sensing applications, directional beamforming enables a radio transceiver to spotlight on a desired subject, thereby reducing static multipath interference and dynamic interference, and improving the sensing reliability [36, 46]. Unfortunately, these 3 advantages are inaccessible for the majority of today's IoT devices, which have to be equipped with only one or two antennas due to cost and form factor constraints. Even for high-end MIMO antenna arrays, their directional beams can only be steered towards line-of-sight (LoS) angles, and cannot easily cover subjects around the corner [39].

Recent research has attempted to bring beamforming capabilities to low-profile IoT devices by deploying a smart surface around. For instance, LAIA [30] builds a wall of antennas which can refocus the signals coming from IoT transmitters. RFocus [11] employs reconfigurable RF switches and antenna elements to form a rectangular

array, which can direct signals towards an intended receiver. While these systems can realize beamforming gains, their form factor is formidable. For example, RFocus uses 3200 antenna elements, spanning a 6 m^2 area, to achieve a 9 dB median beamforming gain for Wi-Fi links.

In this paper, we ask the following question: Can we design a more area-efficient smart surface to enable the aforementioned beamforming capabilities? We propose an affirmative answer through RFlens, a reconfigurable metasurface (MTS) that can "reshape" and resteer the RF signals going through it. The basic working principle of RFlens is shown in Figure 1. RFlens consists of many *unit-cells*, each comprised of two PIN diodes placed in the same orientation. When a bias voltage is applied to PIN diodes, the unit-cell acts as a 1-bit phase shifter (e.g., 0 or π). RFlens can reconfigure the phase coding patterns to manipulate the electromagnetic waves going through the metasurface, and achieve beamforming, multi-beam, and beam steering/resteering.

To build RFlens in practice, we have to address the following non-trivial challenges.

Challenge 1: How to realize a compact metasurface with high beamforming gain? When passing through the metasurface, the incident signals experience reflection attenuation (RA) and transmission attenuation (TA). To reduce the RA, we need to design an efficient metasurface structure whose resonance frequency matches the incidental waves. On the other hand, using materials with a smaller dielectric constant can reduce the TA, but increase the fabrication cost. To balance these design trade-offs, we model the relation between the unit-cell geometry and signal characteristics (i.e., frequency, phase, and amplitude). The model helps optimize the system parameters, including the dielectric substrate, the size of the patch, the size of the slot, the diameter of the metallized via, and the thickness of the dielectric substrate. It ultimately leads to a unit-cell structure with low RA and TA on the 5 GHz ISM band.

Challenge 2: How to enable versatile MIMO-like beam reshaping by reconfiguring the unit-cells? An intuitive solution is to reconfigure each unit-cell with a predefined phase coding pattern, just as in classical delay-and-sum beamforming for phased antenna arrays. But this will result in: 1) High sidelobe due to the low (binary) phase resolution; 2) Low beamforming gain since RFlens arranges the unit-cells into subarrays to construct the metasurface. We instead devise a beam synthesis optimization (BSO) scheme to achieve narrow beamwidth, low sidelobes, and enable versatile multi-beam patterns. The high-level idea is to iteratively adjust the phase coding pattern in order to approach the desired beam pattern. Unfortunately, it is extremely time-consuming for the iterations to converge, as the search complexity grows exponentially with the number of unit-cells and elements per unit-cell. To overcome this hindrance, we seek the optimization using the continuous phase shifting values in classical phased array beamforming, which substantially accelerates the computation.

Challenge 3: How to beamform toward passive subjects, to enable directional or non-line-of-sight (NLoS) wireless sensing applications? RFlens can enable single-antenna wireless sensing devices to beamform towards a subject of interest, and isolate multipath or environmental interference. It can even resteer signals to detour NLoS blockage, thus enabling around-the-corner sensing applications. Yet, the metasurface itself is unaware of the subjects'

locations, and cannot directly coordinate with the sensing devices. We thus propose a simple method to deduce the optimal phase configurations for the metasurface elements that maximize the desired sensing signal SNR. Our basic observation is that each predefined phase coding pattern corresponds to a main angular radiation region. We can thus quantize the region of interest into multiple angles, identify the metasurface configuration for each, and quickly scan across the corresponding beams. Our current RFlens prototype can continuously scan 37 beams within only 150 μs, which covers the half-space with 5° resolution.

We build an RFlens prototype with 16×16 unit-cells spanning an area of $0.484 \times 0.484 m^2$. Extensive experiments demonstrate that RFlens can perform accurate beam steering within a $[-60°, 60°]$ field-of-view. The gain is symmetrical for both forward and reverse direction links. Even with the small-size prototype, RFlens enables up to 9.3 dB signal strength improvement. The median gain is 4.6 dB in the indoor environment and 5.5 dB for long-range outdoor LoS scenarios. We also conduct case studies for communication and sensing applications, which demonstrate that RFlens can improve the secrecy capacity of IoT links by 7.6× on average; it can also improve NLoS sensing performance and mitigate the multi-user interference for activity sensing.

The main contributions of RFlens can be summarized as follows. RFlens represents the first WiFi-band metasurface design that manipulates the phase of penetrating signals to attain beamforming gains at a small physical area. We empirically model the relation between unit-cell geometry and signal characteristics (i.e. frequency, phase, and amplitude) to minimize the transmission loss. In addition, we devise a beam synthesis optimization (BSO) scheme to create multi-beam patterns with narrow beamwidth and lower sidelobe level. Finally, we validate the implementation of RFlens for both communication and sensing applications with comprehensive experiments.

2 RELATED WORK

Antenna array beamforming. Much research has been devoted to using antenna arrays at RF endpoints to improve communication quality. For example, BigStation [52] employs 15 PC servers as a baseband processing unit to drive a 12-antenna RF front-end, to achieve 6.8× link capacity gains. SWAN [50] stitches many antennas to the original RF chains to achieve transmission diversity. Other researchers utilize many antennas to build large-scale MIMO systems [21, 25, 37] or reconfigurable phased arrays [27, 44, 58] to improve link SNR or spatial reuse. These systems are usually bulky and costly, and need to tightly integrate the antennas, RF front-end, and baseband hardware. RFlens follows a different design goal: It serves as a companion smart surface to empower existing low-profile IoT devices. Owing to the modularized unit-cell design, it can potentially be scaled to enable massive MIMO-like fine beamforming capabilities for single- or few-antenna devices.

Smart surfaces. Smart surfaces are gaining traction as a way to "smarten" the radio environment and enhance wireless link quality [13, 42, 47, 48, 57]. MoVR [5] utilizes a programmable millimeter-wave (mmWave) reflector to align the antenna beams under blockage scenarios. It relies on the location sensors on virtual reality devices to assist beam alignment. LAIA [30] exploits large antenna

arrays equipped with programmable, continuous phase shifters to align the phase of different RF paths, thus improving link SNR. RFocus [11] is another smart surface, which achieves beamforming by configuring the signal to either pass through or reflect from the surface element by setting the "on" or "off" state of each element. RFocus only uses a part of unit-cells, and only redirects a fraction of the signal energy. In contrast, RFlens uses the 1-bit phase shifters on all unit-cells simultaneously, and aligns the phase of each unit-cell to achieve beamforming. Thus, RFlens is more area-efficient, i.e., it can achieve a larger beamforming gain with the same physical area. ScatterMIMO [22] utilizes an area-efficient surface to generate virtual AP and enhances the signal power of reflected path power to improve throughput, but only works in five Wi-Fi channels at 5 GHz. Unlike ScatterMIMO, RFlens works well over the whole 5 GHz channels, and enables more versatile beamforming functions such as resteering and splitting, which can be used for multicast, NLoS sensing, etc.

Metamaterials. Metamaterials are three-dimensional, periodic, and artificial structures assembled using conventional composite materials. Metasurfaces can be considered as a class of metamaterials that take the form of a surface. They can be designed to manipulate and interact with electromagnetic waves in unique ways [24, 28, 31, 32, 49]. For example, Li *et al.* [29] utilize an 81-element single-layer reflect-array to perform reflective beamforming. Arbabi *et al.* [9] leverage dielectric metasurfaces to achieve beam polarization. Such beamforming functions are fixed at manufacturing time. Further, some studies [6, 14] apply air gaps in the unit-cell structure to achieve beam steering with a low transmission loss. However, the air gaps will increase design complexity, fabrication complexity, and form factor. Unlike these approaches, RFlens uses a tightly connected multi-layer unit-cell structure. Another series of works [17, 35, 55, 56] demonstrated programmable metasurfaces using PIN diodes. While these approaches have shown great promise to control electromagnetic waves, they mostly focus on the theoretical modeling and simulation verification, and are optimized for a single frequency point or a narrow bandwidth. In contrast, RFlens aims to achieve a low transmission loss when the incident signals span the whole 5 GHz Wi-Fi frequency band. RFlens targets both the IoT communication and sensing use cases, whereas prior work mostly focused on the electromagnetic aspects.

A few practical metasurface designs have emerged recently to enhance wireless link quality. LLAMA [18] uses a programmable metasurface to change the polarity of incident waves and remove the polarization mismatch between transceivers. mmWall [19], most closely related with RFlens, achieves beam steering and splitting for mmWave links. It imposes different voltage values to control a varactor within each unit-cell to realize continuous phase changes, which requires a precise and sophisticated DC voltage control backend. In contrast, RFlens chooses to use PIN diode to change the unit-cell's phase, which only needs binary DC voltage levels. Although the phase resolution of PIN diode is not as good as the varactor diode, RFlens still can achieve good beamforming and beam scanning performance by employing a large number of unit-cells (More details are in Section 4.4). In addition, mmWall focuses on the theoretical modeling and simulation of a high frequency (24-27 GHz) metasurface, whereas RFlens builds a practical system
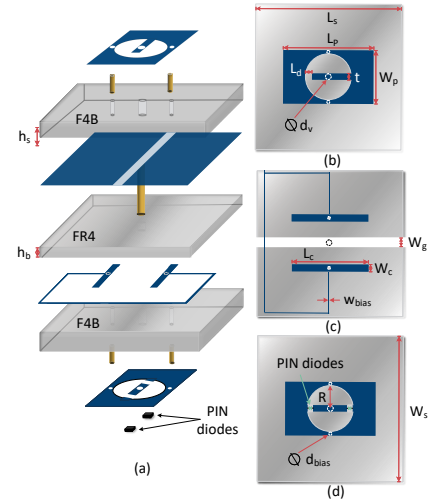

Figure 2: (a) 3D architecture of the proposed unit-cell, (b) upper layer, (c) middle layer, (d) lower layer.

at the 5 GHz Wi-Fi frequency band with an entirely different RF front-end.

3 METASURFACE CONFIGURATION

In this section, we present the detailed design of RFlens, including the basic unit-cell and metasurface architecture.

3.1 Unit-cell Design

To build a compact MTS with high beamforming gain, a unit-cell design should meet two requirements: (i) Each unit-cell can dynamically and independently adjust the phase when an RF wave penetrates it; and (ii) The signals going through the unit-cell should experience a low transmission loss. We now introduce our solutions to meet the requirements.

3.1.1 Designing the unit-cell with phase shifting capability. We use PIN diodes as the basic hardware elements to realize phase shifting. Unlike the varactors used in recent work (Sec. 2), a PIN diode only requires two different DC voltage levels (e.g., 0 V or 5 V) rather than precise and continuous voltage values, which reduces the design complexity and insertion loss while improving the stability [34]. Figure 2 illustrates the 3D structure of a unit-cell. Each unit-cell consists of four metallic layers printed on two identical dielectric substrates. The upper surface of the upper dielectric substrate is printed with rectangular patch antennas loaded by a C-slot (referred to as the *passive patch*). The lower surface of the lower dielectric substrate is printed with a patch antenna of the same size loaded by an O-slot (referred to as the *active patch*). The passive patch is connected to the ground plane through two vertical via-holes. The active patch is connected to a narrow bias line through two vertical via-holes similar to the passive patch. Both patch antennas are connected by a via-hole located at their center.

We place two PIN diodes with the same orientation on the active patch layer as shown in Figure 3(b). The bias current supported by a DC voltage regulator flows from the bias line and flows to the active patch through two vertical via-holes. Then, it flows to the passive patch through a via-hole located at the center after
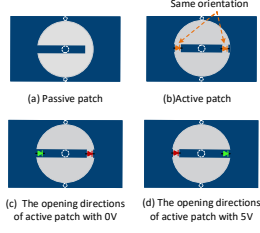
(a) Passive patch (b)Active patch

(c) The opening directions of active patch with 0V (d) The opening directions of active patch with 5V

Figure 3: The opening directions of active patch.

(a) The phase and S_{21} efficiency of the original unit-cell.

(b) The S_{21} efficiency of the original and optimized unit-cell.

(c) The phase of the original and optimized unit-cell.

Figure 4: The phase and S_{21} efficiency of the original and optimized unit-cell.

passing through PIN diodes (Figure 9). Under the different DC voltage levels, the PIN diodes switch to an opposite state and thus the opening directions of the upper and lower patches are opposite or uniform, as shown in Figure 3. Depending on the sign of the bias current, the unit-cell introduces a phase shifting of 0 or π. Therefore, we can consider the unit-cell as a one-bit phase shifter, i.e., zero phase ("0\OFF" state) or 180-degree phase ("1\ON" state), corresponding to two opposite electromagnetic responses. In order to independently adjust each unit-cell's phase, we employ a bias line layer to control the states of the PIN diode within each unit-cell. The detailed schematic of the bias line layer is described in Section 3.2. To analyze the phase and transmission coefficient (i.e., S_{21}) of the unit-cell, we use High Frequency Structure Simulator (HFSS) simulation software to simulate an infinite array of unit-cells. The result is shown in Figure 4(a), we can clearly see that, for signals between 5 GHz and 6.5 GHz, our unit-cell design can effectively alter the phase between 0 and $180°$. Unfortunately, the transmission efficiency is too low (< -3 dB) for signals above 5.2 GHz. We now introduce further steps to counteract this limitation.

3.1.2 Transmission loss optimization. When RF signals impinge on the unit-cell, reflection attenuation (RA) occurs if their resonant frequencies mismatch. We find that the RA is highly correlated with the geometric parameters of the unit-cell. On the other hand, the transmission attenuation (TA) depends on the material of the unit-cell. We can thus focus on these two parameters in order to achieve a low transmission loss.

First, we need to select a substrate material with a low loss property to reduce the TA. The material's property is determined by two factors, i.e., dielectric loss tangent δ and dielectric constant ϵ_r. A lower δ and ϵ_r means lower loss, but higher cost. For example, Rogers Duroid RT6002 ($\delta = 0.0012$ and $\epsilon_r = 2.94$) and Arlon Cu-CLAD 6700 ($\delta = 0.0025$ and $\epsilon_r = 2.35$) have a low transmission loss, but they are expensive (e.g., Rogers costs $1,076 per square meter [3]), making them impractical to commercialize as consumer products. To balance the cost and transmission attenuation, RFlens adopts a cheap F4B ($\delta = 0.002$ and $\epsilon_r = 2.65$) as the material of the upper and lower substrate, and FR4 ($\delta = 0.015$ and $\epsilon_r = 4.2$) as the intermediate substrate (e.g., F4B costs 85 USD per square meter), as shown in Figure 2.
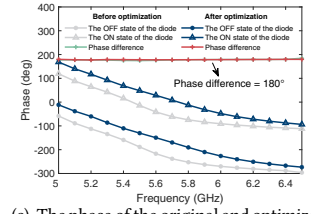
Second, we need to identify the key parameters that impact the resonance frequency of the unit-cell. To this end, we build an equivalent circuit model for the unit-cell (Figure 5), which consists of three key parts, i.e., active patch, passive patch, and T-network. The active patch (Figure 2 (d)) contains an O-structure microstrip
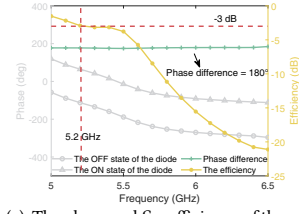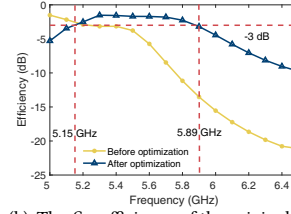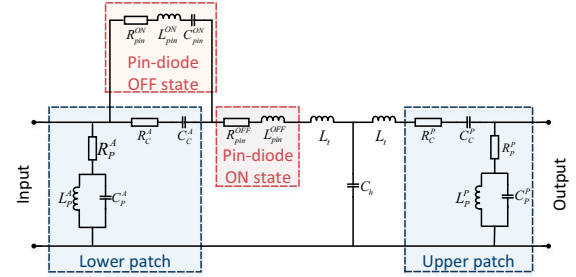

Figure 5: Circuit schematic of the unit-cell.

patch and an O-structure slot. The passive patch (Figure 2 (b)) contains a C-structure microstrip patch and a C-structure slot. We can model the C-structure and O-structure microstrip patch as a combination of a shunt parallel *RLC* resonator and a series complex impedance [16], i.e., $Z_P^{A,P} \equiv \left(R_P^{A,P}, L_P^{A,P}, C_P^{A,P} \right)$. To further illustrate the relationship between the unit-cell's geometric parameters and the circuit model, Z_P^A is derived using the cavity model [23, 38]. Note that Z_P^P and Z_P^A are the same, thereby we only analyze Z_P^A below:

$$Z_P^A = \frac{1}{R_P^A} + \left[j\omega C_P^A + \frac{1}{j\omega L_P^A} \right]^{-1}, \quad (1)$$

where $C_P^A = \frac{\epsilon_0 \epsilon_r L_P W_P}{2h_s} \cos^{-2}\left(\frac{\pi y_0}{L_p} \right)$, $L_P^A = \frac{1}{(2\pi f_1)^2 C_P^A}$ and $R_P^A = \frac{Q_1}{2\pi f_1 C_P^A}$. ϵ_r is the dielectric constant of the dielectric substrate, L_p and W_p is the patch size, h_s is the thickness of the dielectric substrate, f_1 is the resonance frequency, Q_1 is the quality factor [23], and y_0 is the distance of the excitation point from the closest radiating edge. The resistance R_P^A corresponds only to the loss in the radiating elements. The superscripts denote the passive patch and the active patch layer, respectively. The subscripts "P", "C" and "O" stand for "Patch", "C-structure" and "O-structure", respectively.

In addition, the C-structure slot and O-structure slot on the rectangular patch can be equivalent to a resistor (i.e., R_C^A and R_O^P) and a capacitor (i.e., C_C^A and C_O^P) in series as shown in Figure 5. The impedance is expressed as Z_C^A or Z_O^P, respectively. Here, we only analyze Z_C^A because Z_C^A and Z_O^P are identical in theory. Then, the total impedance of the active patch Z^A can be expressed as $Z^A = \frac{Z_P^A + Z_C^A}{Z_P^A Z_C^A}$, where $Z_C^A = R_C^A + \frac{1}{j\omega C_C^A}$. Hence, through the above equations, we can identify two key parameters that determine the resonance frequency: *the size of the patch and slot structure.*
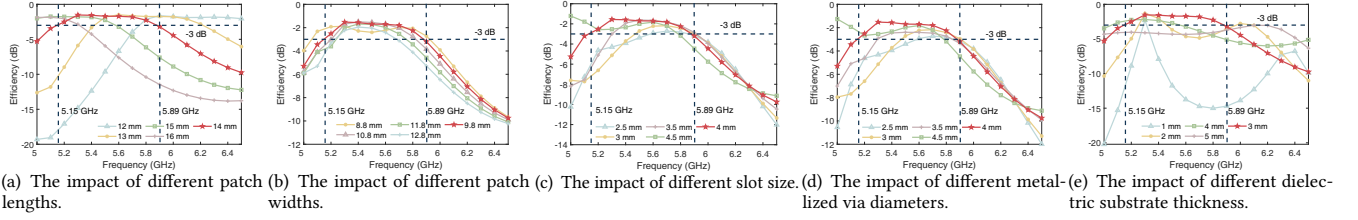
(a) The impact of different patch lengths.
(b) The impact of different patch widths.
(c) The impact of different slot size.
(d) The impact of different metallized via diameters.
(e) The impact of different dielectric substrate thickness.

Figure 6: Different parameters have different effects on the transmission loss.
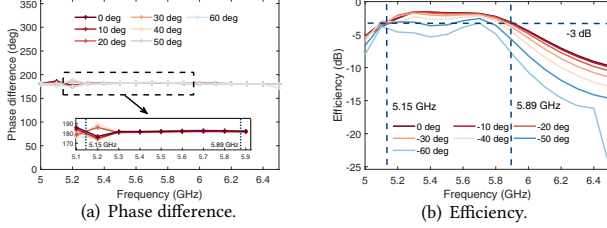

(a) Phase difference.
(b) Efficiency.

Figure 7: Impact of different incidental signal angles.

Since the two patches are connected by the metallized via, we model it as a T-network (L_t, C_h, L_t) as follows [23]:

$$L_t = \frac{\mu_0 h_s}{2\pi} \ln\left(\frac{2C}{\pi C d_v \sqrt{\varepsilon_r} f_1}\right), \quad C_h = \varepsilon_0 \varepsilon_r 2\pi \frac{h_g}{\ln\left(\frac{W_g}{d_v}\right)}, \quad (2)$$

where h_s is the thickness of the substrate, C is the Euler's constant, μ_0 is the magnetic permeability of free space, d_v is the diameter of the metallic via, W_g is the width of the opening in the ground plane, and h_g is the thickness of the ground place. In our implementation, $h_g = 0.035$ mm. Through the above equations, we can identify two key parameters that determine the resonance frequency: *the thickness of dielectric substrate and the diameter of metallized via.*

To explore how they affect the unit-cell's transmission loss across the 5 GHz Wi-Fi band, we use HFSS again to conduct comprehensive simulations and summarize the results below.

(i) The size of patch: The results in Figure 6(a) and Figure 6(b) show that the patch size impacts not only the transmission efficiency but also the frequency response. Figure 6(a) indicates that *a longer patch length leads to lower resonance frequency.* Specifically, the resonance frequency shifts from 6.2 GHz to 5 GHz as the patch length decreases, and the patch length significantly affects the total frequency range that satisfies the > -3 dB transmission efficiency. Therefore, an appropriate patch length could help to keep a low transmission loss for the unit-cell. In our system, we set the patch length to 14 mm.

Figure 6(b) implies that *the wider the patch width, the smaller the resonance frequency bandwidth (> -3 dB).* For example, the bandwidth of the 9.8 mm patch width is 0.84 GHz, larger than the bandwidth of 12.8 mm patch width (i.e., 0.45 GHz). When the width is smaller than 10.8 mm, the bandwidth can cover the whole Wi-Fi frequency band. Due to the average efficiency of 8.8 mm is smaller than 9.8 mm in the whole Wi-Fi frequency band, we choose 9.8 mm in our implementation.

(ii) The size of slot: The result of different slot sizes is shown in Figure 6(c), we can see that *as the size of slot increases, the frequency bandwidth(> -3 dB) increases.* To ensure the efficiency of whole 5 GHz Wi-Fi frequency band is larger than -3 dB, we select 4 mm as the slot's size.

(iii) The diameter of the metallized via: Different via diameters impact both the center resonance frequency and transmission efficiency, which is evident in Figure 6(d). *As the diameter increases, the center resonant frequency decreases, whereas transmission efficiency increases.* We empirically set the via diameter to 4 mm to meet the -3 dB transmission loss in 5 GHz Wi-Fi band.

(iv) The thickness of the dielectric substrate: Figure 6(e) plots the simulated results with different substrate thicknesses. We can see that *the thickness has a significant effect on both the transmission efficiency and resonance frequency.* To meet the requirement of high efficiency at the whole 5 GHz Wi-Fi frequency band, we select 3 mm as substrate thickness to achieve low transmission loss.

Table 1 summarizes the optimal unit-cell parameter configurations based on the above observations (More details are shown in Appendix A). The simulation results in Figure 4(b) demonstrate that the transmission efficiency always exceeds -3 dB under this parameter setup, across the entire 5.15-5.89 GHz band. For phase changes of two states for PIN diodes, Figure 4(c) shows that the absolute phase value of each PIN diode's state changes as the frequency varies, but the phase differences of the "ON" and "OFF" states always keep stable at $180°$.

To explore the impact of different incident angles, we vary the angle from $0°$ to $60°$, and use HFSS to simulate an infinite array of unit-cells. The simulated results are shown in Figure 7. We can clearly see that: (i) the phase differences are stable at $180°$ across the entire 5 GHz Wi-Fi frequency band as the incidental angle changes. This reason is that the phase difference only depends on the two opposite electromagnetic responses. In other words, no matter how the incidental angle changes, the phase difference between two different DC voltage levels, resulting in the opening directions of the upper and lower patches are opposite or uniform, remains $180°$ (More details are given in Section 3.1.1); (ii) the transmission efficiency decreases as the incidental angle increases. This is because the effective MTS aperture area is reduced, which agrees with previous research [17]. When the incidental angle increases to $50°$, the transmission loss still meets the -3 dB requirement across the whole 5 GHz Wi-Fi band. It exceeds -3 dB as the incidental angle goes beyond $60°$. Thus, to maintain high performance, the incident angle is better kept within the $50°$.

3.2 Metasurface Control

Our current prototype of RFlens comprises 256 unit-cells in a 16 × 16 layout, as shown in Figure 8. To dynamically reconfigure the PIN diode states of each unit-cell, a bias line is needed to feed
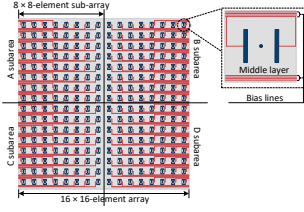
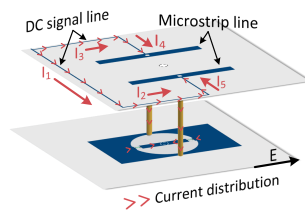**Figure 8: Top view of metasurface with bias lines.**

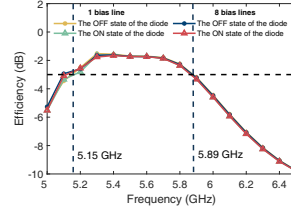**Figure 9: Current distribution on the patch of the unit-cell.**

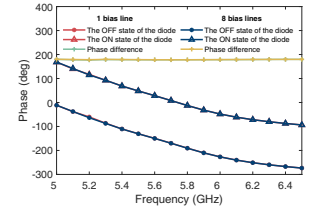**Figure 10: Simulated efficiency about 1/8 bias lines.**

Figure 11: Simulated phase about 1/8 bias lines.

different DC bias voltages (e.g., 0 V or 5 V). When the bias voltage is applied, the current on the activate patch can be perturbed by the corresponding DC current, resulting in RF signal power leaking through the bias lines. The leakage is exacerbated with a large number of bias lines passing through an active patch, leading to a sharp drop in the cell frequency response.

To tackle this challenge, we optimize the RF/DC decoupling through two steps. First, we partition the whole MTS into 4 areas (e.g., A, B, C and D), so the maximum number of bias lines passing through a unit-cell is reduced from 16 to 8. Second, we carefully design a bias circuit involving a DC signal line and two quarter-wavelength microstrip lines. When a bias voltage is applied to the DC signal line, it will generate current, and the current induces coupled electric field. As shown in Figure 9, the electric field coupled by the bias lines L_2 and L_3 is parallel to the electric field of patch, whereas the electric field coupled by L_1 is orthogonal to it. The coupling effect induced by L_2 and L_3 degrades the frequency response. To mitigate this impact, we deploy the L_2 and L_3 bias lines at the edge of the unit-cell. Besides, we design two quarter-wavelength microstrip lines at two via holes to choke the RF signal which enters the bias line.

To verify the effectiveness of the proposed method, we conduct simulation experiments and study the impact of the bias lines on the cell frequency response. As shown in Figure 10 and Figure 11, the phase and efficiency remain highly consistent when there are 1 or 8 bias lines on the unit-cell, for all frequencies from 5 GHz to 6.5 GHz, and for both ON and OFF states. These results further confirm that the RF/DC decoupling circuit on the unit-cell provides good isolation between the active patch and the bias lines.

4 BEAMFORMING THROUGH RFLENS

In this section, we explain how to enable versatile beamforming schemes on RFlens.

4.1 Creating a Single Directional Beam

Consider a MTS of RFlens consists of $M \times N$ elements ($M = N = 16$ in our implementation), as illustrated in Figure 12. When an incident electromagnetic wave impinges on the unit-cell located at (m, n), it experiences a propagation distance of $d_{m,n}$, which leads to a phase shift of $\phi_{m,n}^I$:

$$\phi_{m,n}^I = -k_0 d_{m,n}, \tag{3}$$

where $k_0 = 2\pi/\lambda$; λ is the signal wavelength; $m \in [1, M]$ and $n \in [1, N]$. Suppose the desired beamforming direction is (θ_0, φ_0), where θ_0 and φ_0 are the elevation and azimuth angles, respectively. The theoretical phase distribution of the $(m, n)^{th}$ unit-cell in MTS
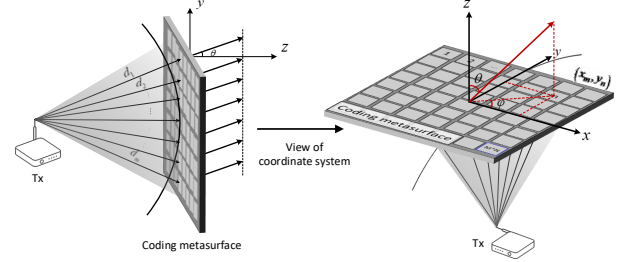

Figure 12: Geometry of the coding metasurface.

should be:

$$\phi_{m,n}^T = -k_0 (x_m \sin\theta_0 \cos\varphi_0 + y_n \sin\theta_0 \sin\varphi_0), \tag{4}$$

where x_m and y_n are the X-axis and Y-axis distances of the $(m, n)^{th}$ unit-cell relative to the origin of coordinate.

Thus, to steer the incident signal to (θ_0, φ_0), the $(m, n)^{th}$ unit should generate a phase compensation of:

$$\phi_{m,n}^C = \phi_{m,n}^T - \phi_{m,n}^I, \tag{5}$$

Recall the unit-cell only provides two phase states ($0°$ or $180°$). To realize the phase compensation, we follow a quantization rule $Q\left(\phi_{m,n}^C |_{1-bit}\right)$ given by:

$$Q\left(\phi_{m,n}^C |_{1-bit}\right) = \begin{cases} 0°, if -\frac{\pi}{2} \leq \phi_{m,n}^C < \frac{\pi}{2} \\ 180°, otherwise \end{cases}, \tag{6}$$

where the $\phi_{m,n}^C$ is the compensated phase.

To verify RFlens can form directional beams despite the quantization effect, we conduct HFSS simulation to analyze the radiation pattern. Figure 13 shows 4 beam patterns generated by ideal continuous phase shifters and the phase of corresponding unit-cells. The blue/gray square represents the $0°/180°$ states, respectively. The maximum directivity is about 20 dB[1] for the main beam with HFSS simulation results, within the $-50°$ to $50°$ primary field of view, as shown in Figure 14. We can see that the main beam direction of the unit-cell design is well aligned with the ideal case, and the sidelobes are relatively small. In fact, we find that the measured average beamforming gain has about 4 dB attenuation compared to simulated results due to the hardware imperfection of MTS, PIN diodes, and the transmitter's antenna (More detailed information in Section 7). In addition, RFlens can beamform towards arbitrary angle (from $-90°$ to $90°$) with a fine-grained $\pm 5°$ resolution. Note that, RFlens can steer the beam both horizontally and vertically. Since most Wi-Fi related communication/sensing use cases have
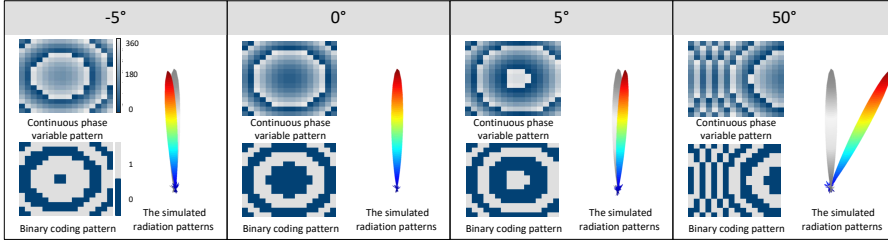
---

[1]The gain of the source antenna is 10 dB.

Figure 13: 3D radiation patterns for several scan angles $(0°, \pm 5°, 50°)$ and corresponding continuous phase variable pattern and binary coding pattern.

Figure 14: Simulated radiation patterns for different scanning angles.

limited freedom in height, we mainly consider the performance within the horizontal plane in this paper.

4.2 Multi-beam Patterns

The ability to "split" incident waves into multiple directional beams can enable unique communication and sensing use cases, such as secure multicast from an IoT sensor and simultaneously tracking the vital signs of multiple human subjects. A straightforward approach to form multi-beam is to divide the whole MTS into subarrays, each independently generating a single beam. But this will hurt the directionality since each subarray only employs a subset of unit-cells. We thus devise a beam synthesis optimization (BSO) scheme. The basic idea is to synthesize a desired multi-beam pattern, by iteratively adjusting the phase states of unit-cells. Without loss of generality, we describe the solution for a dual-beam BSO. Let (θ_1, φ_1) and (θ_2, φ_2) represent two desired directions, BW_1 and BW_2 denote the beamwidths of two mainlobes, and SL is the normalized sidelobe level. To synthesise the desired multi-beam pattern, we first calculate the single beam pattern of (θ_1, φ_1) as below [19]:

$$F_1(\theta_1, \varphi_1) = \sum_{m=1}^{M} \sum_{n=1}^{N} e^{jk_0((x_m u + y_n v) - (x_m \sin\theta_1 \cos\varphi_1 + y_n \sin\theta_1 \sin\varphi_1))},$$
(7)

where $u = \sin\theta\cos\varphi$ and $v = \sin\theta\sin\varphi$, θ and φ vary from $-\pi$ to π. Similarly, we can obtain the single beam pattern F_2 at direction (θ_2, φ_2). Then, the synthetic multi-beam pattern F_s can be calculated as:

$$F_s = \begin{cases} F_1^{norm}(\theta, \varphi), (\theta, \varphi) \in (\theta_1 \pm BW_1, \varphi_1 \pm BW_1) \\ F_2^{norm}(\theta, \varphi), (\theta, \varphi) \in (\theta_2 \pm BW_2, \varphi_2 \pm BW_2), \\ SL, (\theta, \varphi) \in others \end{cases}$$
(8)

where F_1^{norm} and F_2^{norm} are the normalized beam pattern of F_1 and F_2. In this paper, we empirically set $BW_1 = BW_2 = 10°$ and $SL = -40$ dB to achieve a narrow beamwidth and lower sidelobe level.

However, we observe that there exist multiple spikes at the junction of the mainlobe and the sidelobe in the synthetic multi-beam pattern F_s. To mitigate this issue, we adopt a moving average method to smooth synthetic the multi-beam pattern F_s. Next, we randomly generate an initial beam pattern F_g as follows:

$$F_g = \sum_{m=1}^{M} \sum_{n=1}^{N} e^{jk_0((x_m u + y_n v) - (\phi_{m,n}^C + \phi_{m,n}^I))},$$
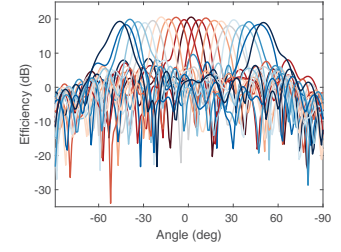(9)

Then, we design a loss function $fitness$ to assess the difference between the generated and desired beam pattern:

$$fit(\theta, \varphi) = \begin{cases} W1 * F_d(\theta, \varphi)^2, (\theta, \varphi) \in (\theta_{1,2} \pm BW, \varphi_{1,2} \pm BW) \\ W2 * F_d(\theta, \varphi)^2, (\theta, \varphi) \in others, \end{cases}$$
(10)

and

$$fitness = \sum fit(\theta, \varphi),$$
(11)

where $F_d = (F_g(\theta, \varphi) - F_s(\theta, \varphi))^2$, W_1 and W_2 are the weighting coefficients. To make the mainlobe of F_g close to the mainlobe of F_s, the values of W_1 and W_2 are set to 100 and 1 respectively, which aims to minimize the mainlobe difference between generated and desired beam pattern.

Finally, we employ a particle swarm optimization (PSO) algorithm [33] to minimize the loss function $fitness$ for finding a solution Φ^* as below:

$$\Phi^* = \arg\min_{\Phi} fitness(\Phi),$$
(12)

where Φ^* is an optimal continuous phase set that can generate the desired beam.

Unfortunately, we find the above iterative optimization is extremely hard to converge, because the particle dimension of PSO is too high (e.g., $M \times N = 256$) which results in a large computational complexity. To accelerate the computation, instead of feeding a random initial phase weight to each unit [15], which causes the loss function to fail to converge in most cases, our key insight is to use the phase coding pattern deduced by the straightforward method (dividing the whole MTS into two subarrays) as the initial values and seed the optimization using the ideal continuous phase set in Eq. (12). The number of convergent iterations is about 20. Finally, the solution Φ^* is put into Eq. (6) to extract the final 1-bit phase coding pattern. Note that we use the BSO scheme to obtain different multi-beam patterns offline. Once obtained, we can build a look-up table (LUT) to store the phase coding patterns. At run-time, we can utilize the LUT solution directly to achieve multi-beam steering.

To demonstrate the effectiveness of the proposed BSO scheme, we simulate a dual-beam case ($-30°$ and $20°$). From the result in Figure 15, we can observe that: 1) the beamwidth of the two mainlobes are narrower than the geometrical method; 2) the sidelobe levels are much lower than the mainlobe levels; and 3) the two mainlobes well match the desired angles.

4.3 How to Find the Beamforming Target?

The MTS of RFlens can be used to beamform towards either a radio receiver in communication use cases, or a passive subject in sensing

use cases. Since the MTS does not know the location of the target, how can it decide on the beamforming direction? A straightforward approach is to try out all possible unit-cell phase configurations, and choose the one that leads to the maximum signal power. But this is infeasible in practice due to the huge dimension of configurations, i.e., 2^{MN}. In RFlens, we leverage the deterministic mapping between the MTS phase configurations and the main radiation regions (i.e., the mainlobe of the beam pattern) to detect the relative direction of the target. The signal power would be maximized when the target is located at the main radiation region.

In communication use cases, we use the maximum received signal power to find the relative direction of transmitter and receiver. Specifically, in our prototype, for simplicity, we synchronize the transmitter with MTS by directly connecting them to the same controller, and let the MTS continuously change 37 phase patterns to perform different radiation patterns from $-90°$ to $90°$ with a fine-grained resolution of $5°$. Then, we collect the signal power values reported by the receiver, and find the maximum signal power to obtain the radiation pattern. Finally, we can deduce the optimal phase configuration. In passive sensing use cases, we can use the above beam steering method to sweep the region of interest, and adopt the strategy of blind beamforming [46] to find the passive target direction.

Note that the control latency of one zone is the same as that of the entire MTS, since the 4 zones are controlled simultaneously. The controller operates at 16 MHz [10], so the control latency of a zone is 4.06 μs, and switching across 37 beam patterns sequentially only takes 150 μs in total. In theory, the end-to-end latency includes beam scanning latency and the feedback latency of per-beam signal strength. Generally, the sector information transmitted between Tx and MTS is about few bytes. To properly account for the feedback latency, we consider two schemes to perform the feedback between the Tx and MTS. The first scheme is to use a high-speed wired connection via a Gigabit Ethernet cable, and the total overhead is about 300 μs. The second scheme is to employ a very low rate wired or wireless connections (e.g., 56 Kbps). The corresponding total overhead is no more than 600 ms. Although RFlens has a relatively large overhead in this case, it has limited impact on performance. This is because our current system mainly focuses on static or quasi-stationary cases, not for high mobility cases.

4.4 Asymptotic Performance of the RFlens Design

In this section, we discuss how well RFlens' beamforming performance scales with the number of unit-cells, and the area efficiency, in comparison to an ideal antenna array with continuous phase shifters.

4.4.1 1-bit Phase Shifter vs. Continuous Phase Shifter. Consider a MTS of RFlens with the default $M \times N$ layout. The array factor [19] of the MTS can be expressed by:

$$F = \sum_{m=1}^{M} \sum_{n=1}^{N} e^{jk_0((x_m u + y_n v))}. \tag{13}$$

To steer the beam pattern toward the desired direction at (θ_0, φ_0), we need to compensate a phase value ϕ_0 for the $(m, n)^{th}$ unit-cell.
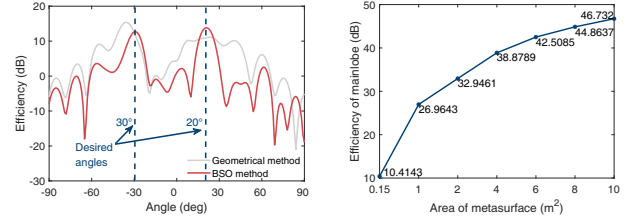

Figure 15: The multi-beam of different methods.

Figure 16: The impact of different areas.

Therefore, the Eq. (13) can be written as :

$$F^{ideal} = \sum_{m=1}^{M} \sum_{n=1}^{N} e^{jk_0((x_m u + y_n v) - \phi_{m,n}^0)}. \tag{14}$$

A quantized Q-bit phase shifter only has 2^Q finite discrete phase values. Note that $Q = 1$ in our simulation. Hence, the phase quantization would introduce phase error, defined as $\phi_{m,n}^{err}$ for the $(m, n)^{th}$ unit-cell. Therefore, the actual array factor becomes:

$$F^{actual} = \sum_{m=1}^{M} \sum_{n=1}^{N} e^{jk_0((x_m u + y_n v) - \phi_{m,n}^0 + \phi_{m,n}^{err})}, \tag{15}$$

where $\phi_{m,n}^{err} = \phi_{m,n}^0 - \phi_{m,n}^q$, and $\phi_{m,n}^q$ is the quantized phase. Clearly, *the generated beam pattern is related to the total number of unit-cells and quantized phase.*

Based on above equations, we simulate the ideal beam pattern with the continuous phase shifter and the actual beam pattern with the 1-bit phase shifter, i.e., unit-cell on RFlens. We observe that the difference in terms of mainlobe angle approaches 0 when the number of unit-cells exceeds 121. The efficiency difference approaches a constant (3.8 dB) when the number of unit-cells exceeds 81. In addition, the -3 dB beamwidth becomes narrower as more unit-cells are employed. To summarize, *in spite of the 1-bit phase quantization, RFlens can achieve a near-ideal beam pattern with accurate direction, high efficiency and narrow mainlobe, as long as it has a large number of unit-cells.*

4.4.2 Area Efficiency. We now examine how RFlens' beamforming performance scales as its physical size increases. Each unit-cell is 0.024×0.024 m^2 by design. For simplicity, we consider a square shaped MTS. Figure 16 shows the numerical simulation result based on Eq. (15). We can see that the efficiency of the mainlobe increases with the MTS area. When the area approaches 6 m^2, the efficiency approaches 42.5 dB, which is 31.5 dB higher than the state-of-the-art RFcous [11] with the same aperture! Hence, RFlens is a much more area-efficient smart surface.

Lessons learned: RFlens can achieve larger beamforming gain and more fine-grained beam steering and multi-beam resolution when the phase shifter resolution and array size are increased. But the design complexity increases with the phase shifter resolution. Meanwhile, more unit-cells mean more PIN diodes, which corresponds to higher cost and power consumption. To balance the trade-off between performance and cost, the current RFlens prototype uses 16×16 1-bit coding unit-cells. The power consumption is only at the level of mW since the MTS itself does not emit any power. Note that the binary phase shifting is independent of the signal's frequency in our system.
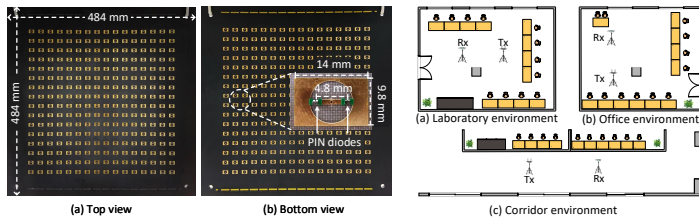
Figure 17: The prototype of RFlens.
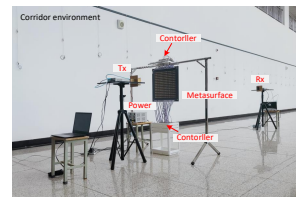

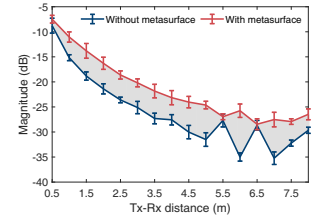**Figure 18: Deployment layout.**

Figure 19: System setup.

Figure 20: The results under different Tx-Rx distances.

5 IMPLEMENTATION

Metasurface configuration. Our MTS prototype is obtained by the following steps: (1) We first design the model of MTS on the HFSS simulation software. (2) Then, we present this model in Autodesk Computer Aided Design (AutoCAD) to export the structure of each layer. (3) Finally, we hand it over to a professional manufacturer for processing and assembly. The final prototype of RFlens is shown in Figure 17. Our current RFlens prototype is made of 256 functional unit-cells with a total surface area of 48.4×48.4 cm^2 and a thickness of 6.2 mm. Each unit-cell has two PIN diodes (SMP1340-040LF [4]). A DC voltage regulator (MESTEK DP3005B [2]) supplies the biasing voltages to the MTS.

RFlens Control. RFlens adjusts each PIN diode pair's state independently by switching the bias voltage between 0 V (OFF state) and 5 V (ON state). To control the bias voltages for all the unit-cells, we design a control circuit module consists of two Arduino Mega2560 controllers and 32 74HC595 shift registers. We divide the entire MTS board into 4 zones with each zone including 8×8 unit-cells (Figure 8). Since each shift register outputs 8 bits, we utilize one shift register to simultaneously set the states of 8 individual unit-cells. Further, we assign 8 shift registers to each zone to control 8×8 unit-cells. By doing so, the setting time for the whole surface decreases by 32 times. Note that unlike the radio relay equipped with an antenna array, RFlens' power consumption is only on the order of mW since the MTS itself does not emit any power.

Experimental setup. For controlled experiments, we use one USRP N210 software-defined radio with a UBX-40 daughterboard as the radio transceiver, operating at a default center frequency of 5.54 GHz. The transmitter transmits a cosine waveform with a bandwidth of 500 KHz, and the sampling rate of the receiver is 1 MHz. The signal processing components are implemented by Matlab and LabVIEW. We conduct extensive experiments in three indoor environments to evaluate the performance of RFlens: an office environment furnished with desks and chairs, a spacious corridor environment and a lab (default setup) environment with furniture like tables and chairs. Figure 18 illustrates the layout of the 3 scenarios and Figure 19 is a practical experiment evaluation scenario in the corridor environment. In the default experimental setting, we set the transmitter-receiver (Tx-Rx) distance as 3 m and the transmitter and metasurface (Tx-MTS) distance as 29 cm. All devices are placed at a height of 1 m. The transmitter is deployed in the normal direction of the MTS.

6 MICRO-BENCHMARK

Verification of beamforming. We conduct experiments under different Tx-Rx distances (from 0.5 m to 8 m by the step of 0.5

m) in the laboratory environment. Figure 20 depicts the received signal strengths with and without using MTS. When the Tx-Rx distance is 6 m, the received signal strength increases by 9.25 dB from -35 dB without MTS to -25.75 dB with MTS. It indicates that the MTS enhances the transmission power a lot by aggregating more energy. When the distance changes, rich multipath in the office environment causes variations in received signal strengths. Nevertheless, RFlens is particularly effective for locations with lower signal strengths that are caused by more severe multipath impact. Therefore, RFlens performs well in beamforming.

Verification of ISM bandwidth control. To verify the effectiveness of RFlens over the entire 5 GHz ISM frequency band, we measure the signal strength by varying the operating frequency from 5.18 GHz to 5.81 GHz with a step of 0.09 GHz in the office environment. The results with MTS and without MTS are shown in Figure 21. The minimum, median, and maximum signal strength increase 2 dB, 4 dB, and 5 dB across the whole band, respectively. It demonstrates that RFlens is capable of boosting signal strength efficiently under a specific frequency. Thus, RFlens can be applied to the ubiquitous commercial IoT devices to realize the benefits of a large antenna array.

Verification of beam steering. We deploy the transmitter at the center of a circle and the receiver on the circle with a radius of 3 m, where the receiver moves along the semicircle from $-90°$ to $90°$ with a step of $5°$. Figure 22 shows the confusion matrix of beam steering results. It proves that RFlens performs accurate beam steering reaching up to a wide range of $120°$, i.e., $[-60°, 60°]$. Figure 23 indicates that the measured beams have a resolution of $5°$ (the mean error is $2.5°$), making fine-grained angular resolution feasible on commercial IoT devices. Moreover, the received signal strength of the main beam is 13.3 dB higher than the sidelobe on average. It manifests that RFlens can achieve beamforming in any desired direction. The results of experimental measurements (Figure 22 and Figure 23) are highly consistent with the simulations (Figure 14), verifying RFlens's functionality of dynamic beam focusing.

Verification of dual beams. We respectively select desired symmetric angles and asymmetric angles from $-50°$ to $50°$, and configure the MTS with corresponding phase coding to estimate beam patterns. The results are shown in Figure 24 and Figure 25. The peaks of estimated beam patterns have an average error of $3°$ compared to the ground truths. It demonstrates RFlens works well in both symmetric and asymmetric beams. Besides, the -3 dB beamwidth of the main lobe becomes wider and has lower energy when the separation between two beams gradually increases. The reason is that the big angular interval of the main lobes makes that each unit difficult to coordinate simultaneous gains in both
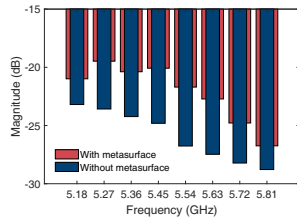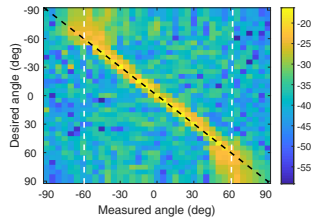
Figure 21: The performance over 5 GHz ISM bandwidth.

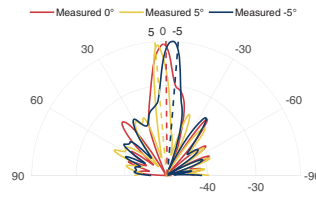**Figure 22: The results of beam steering from −90° to 90°.**

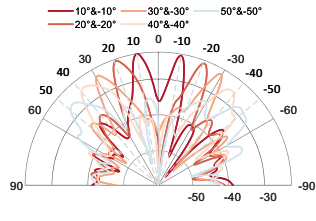**Figure 23: The resolution of beam patterns with MTS.**

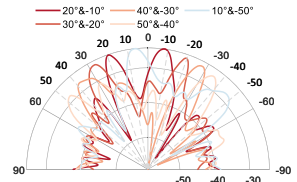**Figure 24: The performance of symmetric dual beams.**
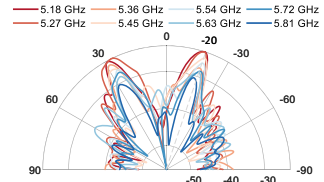

Figure 25: The performance of asymmetric dual beams.

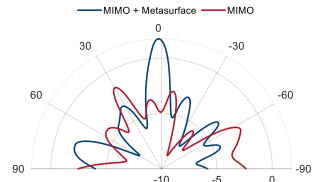**Figure 26: The results of dual beams over 5 GHz bandwidth.**

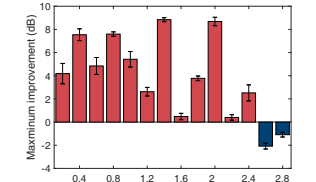**Figure 27: The performance of beam resteering.**

Figure 28: The results under different Tx-MTS distances.

directions. Furthermore, we vary the frequency from 5.18 to 5.81 GHz to study the dual beams capability in different frequencies, the results are illustrated in Figure 26. It shows that RFlens still can precisely direct the beam to desired orientations but have a decreased signal strength as the frequency increases.

Verification of beam resteering. We use a 4-antenna WARP software radio as a transmitter and a single-antenna WARP board as a receiver to examine the beam resteering performance under this MIMO setup. The Tx-Rx distance is set as 3 m and a barrier wall decorated with absorber material is deployed at the LoS link with 70 cm away from the transmitter. First, we perform beam precoding at the transmitter to focus on a direction of 30°, and move the receiver from −90° to 90° with a radius of 3 m to collect 30 measurements. Then, we set a −30° phase coding pattern, put the MTS aside along the barrier wall and move the receiver to re-collect 30 measurements. Figure 27 shows that RFlens can precisely resteer the transmission beam from 30° to 0°. Besides, RFlens improves signal strength by 3.5 dB based on the beamforming. This is particularly useful to help the receiver in the "corner" to hear the transmitter "sound".

7 EVALUATION

7.1 Performance Benchmark

Different transmitter and metasurface distances. We increase the transmitter-metasurface (Tx-MTS) distance from 0.2 m to 2.8 m by the step of 0.2 m to evaluate the maximum signal strength improvement provided by the MTS. Under each Tx-MTS distance setting, we place the receiver in a position to get the maximum received signal strength by taking the average of 20 experiments, and measure the signal strength without MTS as the baseline. The improvements between the maximum signal strengths and baseline measurements are presented in Figure 28. It shows that RFlens works well with the Tx-MTS distance up to 2.4 m. A negative improvement appears when the distance is bigger than 2.4 m. In other words, the maximum improvement is less than 0 dB when the distance is larger than 2.4 m. This is because the current size of the

metasurface (48.4×48.4 cm^2) is small compared to the Tx-MTS distance, so the compensation phase becomes smaller than the 1-bit quantization interval. Consequently, the values of phase coding pattern become all 0s or 1s, and the MTS is unable to effectively align the phase of the RF signals. This issue can be solved by increasing the number of unit-cells [51] or using a finer grained phase quantization method [20].

Different environments. To evaluate the performance of RFlens in different environments, we conduct extensive experiments in the laboratory, office, and anechoic chamber, respectively. The deployment setup is the same as the office scenario depicted in Section 6. We measure the received signal strengths under different transmitter-receiver (Tx-Rx) distances and calculate the signal strength gains offered by the MTS. The results are shown in Figure 29. In the anechoic chamber, the signal strength improvements under different Tx-Rx distances are relatively stable around 5 dB. In the laboratory and office, almost all the improvements are above 0 dB and up to 9.2 dB. It demonstrates that RFlens performs efficiently under random multipath impacts in different environments.

Fault tolerance. The unit-cells are built from inexpensive PIN diodes and some may inevitably fail over time. To verify the MTS robustness, we manually disable a random subset of unit-cells (from 0 to 256 by the step of 16) and measure the received signal strength. Figure 30 depicts the signal magnitude under a different number of disabled unit-cells. The blue-dash line shows the reference magnitude without using a MTS. The beamforming performance decreases gradually when the number of disabled unit-cells increases. The magnitude value goes down to 0 when there are more than 176 disabled unit-cells. With more than 70% disabled unit-cells, the MTS serves as a "wall" that attenuates the signal. But in most common cases with a few unit-cells disabled, RFlens still achieves high gains.

7.2 Communication Use Cases

Improving link capacity and throughput. We investigate the link capacity improvement induced by RFlens' beamforming capability in the laboratory environment. The Tx-Rx distance is increased from 0.5 m to 8 m by the step of 0.5 m and the TX-MTS
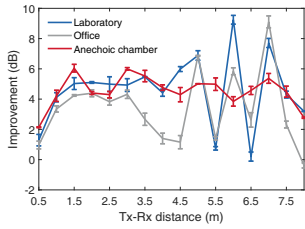
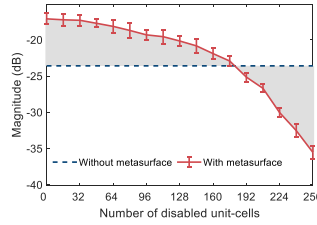**Figure 29: The results under different environments.**
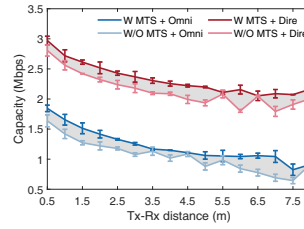

Figure 30: The performance of fault tolerance.
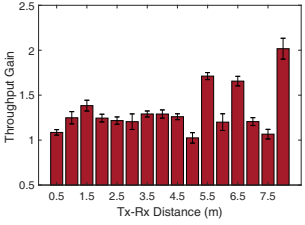

Figure 31: The performance of channel capacity.
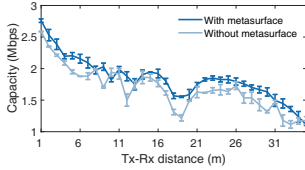

Figure 32: The performance of throughput gain.

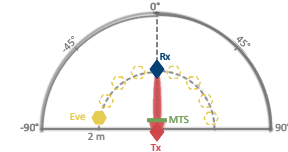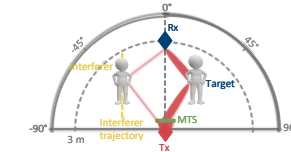**Figure 33: Long-range performance.**

Figure 34: RFlens for Security Analysis.

Figure 35: RFlens for interference sensing.

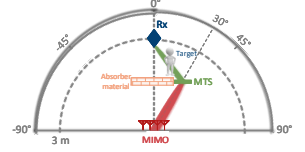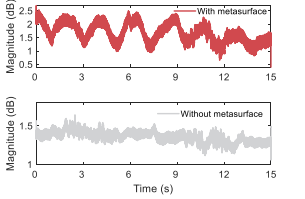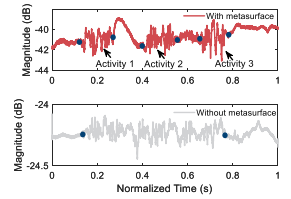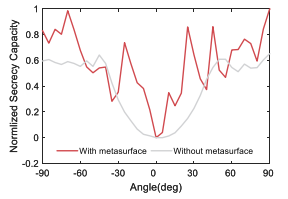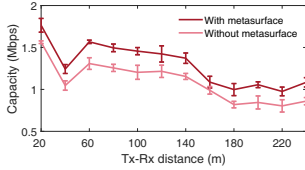**Figure 36: RFlens for NLoS sensing.**

distance is set as 29 cm. In each location, we collect 20 measurements and calculate the average link capacity. The results of using the omnidirectional/directional antenna (referred to Omni and Dire) and with/without the metasurface (referred to W MTS and W/O MTS) are shown in Figure 31. It reports that with the help of MTS, the absolute link capacities for both antennas are large and stable as the distance increases. While the relative capacity gains for two antennas are inconsistent due to the various baseline capacities caused by multipath interference. Indeed, RFlens can also improve the transmission signal power of reverse link because the waves propagating in the reverse link interact with the electromagnetic response induced by RFlens in the same way as the waves propagating in the forward link. In addition, RFlens can also improve channel gains for the commercial Wi-Fi device.

We now evaluate the throughput improvement induced by RFlens' beamforming capability in the lab environment by varying the Tx-Rx distance from 0.5 m to 8 m, while keeping the Tx-MTS distance at 29 cm. Two laptops equipped with an Intel 5300 Wi-Fi NIC and a directional antenna act as the Tx and Rx, respectively. The Wi-Fi devices are configured to 149 with a 40 MHz bandwidth centered at 5.72 GHz. At each location, we repeat an iperf2 TCP session 20 times over the WiFi link and measure the throughout gain relative to the baseline without the MTS. The results are shown in Figure 32. Although the throughput gain varies due to the unpredictable multipath effect, RFlens achieves a 1.33× improvement on average (2× maximum) compared to the case without the MTS. The experiment demonstrates the effectiveness of the RFlens in boosting the end-to-end performance of a wireless network.

We further conduct experiments in an outdoor open field and a spacious corridor environment, where the Tx and MTS are fixed and Rx moves away. The transceiver is equipped with a directional

antenna. We collect 20 measurements in each deployment. Figure 33 shows that the outdoor improvement is more stable than the indoor improvement. The capacity is generally improved in indoor environments by the MTS, while the enhancements of different distances are different due to multipath. This result highlights the feasibility of using the MTS to enhance long-range IoT links.

Improving secrecy capacity. We demonstrate how RFlens can help improve the secrecy capacity of the low-profile IoT devices without beamforming capabilities. Specifically, the target Rx is 2 m away from the Tx, and the eavesdropper moves on the semicircle of the transmitter with a radius of 2 m. We follow [12, 53] to evaluate the secrecy capacity C_s, i.e., robustness against eavesdropping. $C_s = 1$ means the eavesdropper is unable to obtain the signal or decode information from the transmitter; $C_s = 0$ means the signal strength at the eavesdropper is as high as that at the target receiver. As shown in Figure 34, although the security performance of RFlens slightly drops in some locations due to multipath, the average and maximum secrecy capacity improvements across $-30°$ to $30°$ are 7.6× and 25.7× by comparing the results with and without the MTS, respectively. Thus, RFlens can reduce the risk of eavesdropping and effectively improve the secrecy capacity.

7.3 Sensing Use Cases

Overcoming interference through directional wireless sensing. Interference from nearby subjects is a well-known challenge in contact-free wireless sensing systems [45, 54]. In order to separate the target-reflected signal from interference signal, traditional methods use a large antenna array for spatial filtering [26, 43] or a large channel bandwidth for time domain resolution [7, 8]. But these approaches are impractical on low-profile IoT devices. In contrast, RFlens works as a companion device for existing IoT devices

to overcome the above limitation. To verify the feasibility, we follow the activity sensing setup in Figure 35. The target performs the "deep squat" three times with and without MTS. Meanwhile, an interferer locates 2 m away from the target, walks back and forth on the line that is perpendicular to the interfere-target connection line. The result shows that RFlens can effectively mitigate the interference and significantly improve the detection accuracy of target activity. The reason is that based on the beamforming ability, the MTS focuses more signal power on the target and enhances the target-reflected signal.

NLoS sensing through beam resteering. A large antenna array can be steered towards LoS angles but cannot effectively cover subjects around the corner. To overcome this issue, RFlens uses MTS as a pass-through relay to resteer the RF signal towards the target for sensing. We take human respiration detection as an example to verify RFlens 's performance. Figure 36 shows a toy example of the NLoS sensing scenario with a MIMO transmitter (4-antenna WARP software radio) and a receiver (single-antenna WARP board) locating at opposite sides of the absorber material covered obstacle. We conduct two rounds of experiments to collect respiration measurements, i) the transmitter performs beamforming toward $0°$, ii) the transmitter first performs beamforming toward $30°$ and then the MTS performs beam resteering toward the target. The results are shown in Figure 36. It indicates that the MTS's beam resteering greatly enhances the reflected signal strength, thus improving the detection accuracy under the NLoS-sensing scenario. Note that the beam resteering ability can also overcome the "blind spots" issue in wireless sensing applications.

8 DISCUSSION

The design of metasurface. With more unit-cells, RFlens can achieve larger beamforming gain and more fine-grained beam steering and multi-beam resolution. To balance the trade-off between the performance and cost, the current RFlens prototype uses $16×16$ unit-cells to build the MTS. Although the current prototype of RFlens still occupies a large space relative to many tiny IoT devices, the advantage of the MTS is that it is a thin surface. So it can potentially be embedded into the facades of environment (e.g., furniture and walls) to reduce the footprint. Also, our design can indeed be applied to the cases where the Tx is a multi-antenna access point or base station. In our micro-benchmark section, we have successfully verified RFlens can work well with a MIMO Wi-Fi AP (Figure 27 and Figure 36), and help it to resteer the beams. We thus will explore how to tailor the MTS size to specific applications in the future. Besides, RFlens selects 1-bit phase coding to compensate each unit but induces a certain phase error. As future work, we will use higher resolution phase coding to reduce the error, or introduce amplitude coding as a complementary method.

Implementation cost. In our prototype, we select FR4 and F4B as substrate materials to form a MTS with an area of $48.4 × 48.4$ cm^2 and a thickness of 6.2 mm. The substrate costs approximately $160 and each PIN diode costs $0.17. The total material cost is $246 whereas fabrication cost becomes negligible for mass production. Overall, the cost is comparable to a MIMO Wi-Fi AP. However, RFlens is much more attractive for IoT use cases. Owing to its much lower power consumption, it can potentially be battery powered

and easily repositioned, e.g., to facilitate different IoT devices in a smart home.

Working frequency band. Our current RFlens is implemented on the 5 GHz Wi-Fi band because 5 GHz is the working frequency band of many WiFi sensing applications such as gesture recognition [59], which need a wide frequency band to achieve high time/range resolution. In addition, many IoT devices such as surveillance cameras reside on the 5 GHz band. Our design can be easily migrated to lower frequencies (2.4 GHz and 900 MHz).

Communication burden. In our current implementation, the Tx and MTS are controlled by the same host, so the low rate control commands are essentially sent through a wired connection. Alternatively, we can employ a simple low-rate wireless control channel (e.g., the wireless link used for handheld remote) between Tx and MTS, and this channel only needs a small bandwidth. The actual implementation is beyond the scope of the current work and left for future exploration.

Moving target scenario. Our current experiments mainly focus on the scenario where the target stays at a fixed position. RFlens can work for quasi-stationary scenarios in general, where the target occasionally moves. In such cases, RFlens only needs to rescan the area to determine the direction of the target. If the target is constantly moving at a fast speed, RFlens needs to scan continuously and may not be able to derive the optimal beam in time. We will leave the high mobility scenario as a challenging yet interesting research direction for future work.

9 CONCLUSION

This paper introduces RFlens, a reconfigurable metasurface that can effectively beamform and resteer the RF signals going through it. RFlens consists of many small unit-cells built by two PIN diodes and each unit-cell acts as a phase shifter. By encoding the phase shifting values, RFlens can manipulate electromagnetic waves. The prototype implementation demonstrates that RFlens can improve the signal strength by up to 9.3 dB, even with a relatively small layout with $16 × 16$ unit-cells. We conduct case studies for communication and sensing applications, which show that RFlens can improve secrecy capacity and enhance the sensing performance in NLoS scenarios.

REFERENCES

[1] [n.d.]. Blink camera for home. https://blinkforhome.com.
[2] [n.d.]. MESTEK-DP3005B. https://www.mestek.com.
[3] [n.d.]. Rogers Duroid RT6002. https://www.surplusgizmos.com/Rogers-RT6002-High-Frequency-Laminate-Sheet_p_738.html.

[4] [n.d.]. SMP1340-040LF. https://www.skyworksinc.com/Products/Diodes/SMP1340-Series.

[5] Omid Abari, Dinesh Bharadia, Austin Duffield, and Dina Katabi. 2017. Enabling high-quality untethered virtual reality. In *14th USENIX Symposium on Networked Systems Design and Implementation (NSDI 17)*. 531–544.

[6] Ahmed H Abdelrahman, Atef Z Elsherbeni, and Fan Yang. 2014. Transmitarray antenna design using cross-slot elements with no dielectric substrate. *IEEE Antennas and Wireless Propagation Letters* 13 (2014), 177–180.

[7] Fadel Adib, Zachary Kabelac, and Dina Katabi. 2015. Multi-person localization via RF body reflections. In *12th USENIX Symposium on Networked Systems Design and Implementation (NSDI 15)*. 279–292.

[8] Fadel Adib, Hongzi Mao, Zachary Kabelac, Dina Katabi, and Robert C Miller. 2015. Smart homes that monitor breathing and heart rate. In *Proceedings of the 33rd annual ACM conference on human factors in computing systems*. 837–846.

[9] Amir Arbabi, Yu Horie, Mahmood Bagheri, and Andrei Faraon. 2015. Dielectric metasurfaces for complete control of phase and polarization with subwavelength spatial resolution and high transmission. *Nature nanotechnology* 10, 11 (2015), 937–943.

[10] ARDUINO. 2021. *ARDUINO MEGA 2560 REV3*. Retrieved March 21, 2021 from https://store.arduino.cc/usa/mega-2560-r3

[11] Venkat Arun and Hari Balakrishnan. 2020. RFocus: Beamforming using thousands of passive antennas. In *17th USENIX Symposium on Networked Systems Design and Implementation (NSDI 20)*. 1047–1061.

[12] Joao Barros and Miguel RD Rodrigues. 2006. Secrecy capacity of wireless channels. In *2006 IEEE international symposium on information theory*. IEEE, 356–360.

[13] Ertugrul Basar, Marco Di Renzo, Julien De Rosny, Merouane Debbah, Mohamed-Slim Alouini, and Rui Zhang. 2019. Wireless communications through reconfigurable intelligent surfaces. *IEEE ACCESS* 7 (2019), 116753–116773.

[14] Binh, Duong, Nguyen, Pichot, and Christian. 2019. Unit-Cell Loaded With PIN Diodes for 1-Bit Linearly Polarized Reconfigurable Transmitarrays. *IEEE Antennas and Wireless Propagation Letters* 18, 1 (2019), 98–102.

[15] D.W. Boeringer and D.H. Werner. 2004. Particle swarm optimization versus genetic algorithms for phased array synthesis. *IEEE Transactions on Antennas and Propagation* 52, 3 (2004), 771–779.

[16] Christophe Caloz and Tatsuo Itoh. 2005. *Electromagnetic metamaterials: transmission line theory and microwave applications*. John Wiley & Sons.

[17] Anjie Cao, Zhansheng Chen, Kai Fan, Yuehui You, and Chong He. 2020. Construction of a Cost-Effective Phased Array Through High-Efficiency Transmissive Programable Metasurface. *Frontiers in Physics* 8 (2020).

[18] Lili Chen, Wenjun Hu, Kyle Jamieson, Xiaojiang Chen, Dingyi Fang, and Jeremy Gummeson. 2020. Pushing the Physical Limits of IoT Devices with Programmable Metasurfaces. *arXiv preprint arXiv:2007.11503* (2020).

[19] Kun Woo Cho, Mohammad H Mazaheri, Jeremy Gummeson, Omid Abari, and Kyle Jamieson. 2021. mmWall: A Reconfigurable Metamaterial Surface for mmWave Networks. In *Proceedings of the 22nd International Workshop on Mobile Computing Systems and Applications*. 119–125.

[20] Fatimata Diaby, Antonio Clemente, Ronan Sauleau, Kien T Pham, and Laurent Dussopt. 2019. 2 Bit Reconfigurable Unit-Cell and Electronically Steerable Transmitarray in Ka-Band. *IEEE Transactions on Antennas and Propagation* 68, 6 (2019), 5003–5008.

[21] Rahman Doost-Mohammady, Oscar Bejarano, Lin Zhong, Joseph R Cavallaro, Edward Knightly, Z Morley Mao, Wei Wayne Li, Xuemin Chen, and Ashutosh Sabharwal. 2018. RENEW: programmable and observable massive MIMO networks. In *2018 52nd Asilomar conference on signals, systems, and computers*. IEEE, 1654–1658.

[22] Manideep Dunna, Chi Zhang, Daniel Sievenpiper, and Dinesh Bharadia. 2020. ScatterMIMO: Enabling virtual MIMO with smart surfaces. In *Proceedings of the 26th Annual International Conference on Mobile Computing and Networking (MobiCom)*. 1–14.

[23] Ramesh Garg, Prakash Bhartia, Inder J Bahl, and Apisak Ittipiboon. 2001. *Microstrip antenna design handbook*. Artech house.

[24] Nathaniel K Grady, Jane E Heyes, Dibakar Roy Chowdhury, Yong Zeng, Matthew T Reiten, Abul K Azad, Antoinette J Taylor, Diego AR Dalvit, and Hou-Tong Chen. 2013. Terahertz metamaterials for linear polarization conversion and anomalous refraction. *Science* 340, 6138 (2013), 1304–1307.

[25] Ezzeldin Hamed, Hariharan Rahul, Mohammed A Abdelghany, and Dina Katabi. 2016. Real-time distributed MIMO systems. In *Proceedings of the 2016 ACM SIGCOMM Conference*. 412–425.

[26] Wenjun Jiang, Hongfei Xue, Chenglin Miao, Shiyang Wang, Sen Lin, Chong Tian, Srinivasan Murali, Haochen Hu, Zhi Sun, and Lu Su. 2020. Towards 3D human pose construction using wifi. In *Proceedings of the 26th Annual International Conference on Mobile Computing and Networking (MobiCom)*. 1–14.

[27] Suraj Jog, Jiaming Wang, Junfeng Guan, Thomas Moon, Haitham Hassanieh, and Romit Roy Choudhury. 2019. Many-to-many beam alignment in millimeter wave networks. In *16th USENIX Symposium on Networked Systems Design and Implementation (NSDI 19)*. 783–800.

[28] Aobo Li, Shreya Singh, and Dan Sievenpiper. 2018. Metasurfaces and their applications. *Nanophotonics* 7, 6 (2018), 989–1011.

[29] Yuezhou Li, ME Bialkowski, KH Sayidmarie, and NV Shuley. 2010. 81-element single-layer reflectarray with double-ring phasing elements for wideband applications. In *2010 IEEE Antennas and Propagation Society International Symposium*. IEEE, 1–4.

[30] Zhuqi Li, Yaxiong Xie, Longfei Shangguan, Rotman Ivan Zelaya, Jeremy Gummeson, Wenjun Hu, and Kyle Jamieson. 2019. Towards programming the radio environment with large arrays of inexpensive antennas. In *16th USENIX Symposium on Networked Systems Design and Implementation (NSDI 19)*. 285–300.

[31] Mingkai Liu, David A Powell, Yair Zarate, and Ilya V Shadrivov. 2018. Huygens' metadevices for parametric waves. *Physical Review X* 8, 3 (2018), 031077.

[32] Shuo Liu, Tie Jun Cui, Quan Xu, Di Bao, Liangliang Du, Xiang Wan, Wen Xuan Tang, Chunmei Ouyang, Xiao Yang Zhou, Hao Yuan, et al. 2016. Anisotropic coding metamaterials and their powerful manipulation of differently polarized terahertz waves. *Light: Science & Applications* 5, 5 (2016), e16076–e16076.

[33] Federico Marini and Beata Walczak. 2015. Particle swarm optimization (PSO). A tutorial. *Chemometrics and Intelligent Laboratory Systems* 149 (2015), 153–165.

[34] Binh Duong Nguyen and Christian Pichot. 2018. Unit-cell loaded with PIN diodes for 1-bit linearly polarized reconfigurable transmitarrays. *IEEE Antennas and Wireless Propagation Letters* 18, 1 (2018), 98–102.

[35] L. D. Palma, A. Clemente, L. Dussopt, R. Sauleau, and P. Pouliguen. 2016. Circularly-polarized reconfigurable transmitarray in Ka-band. In *2016 10th European Conference on Antennas and Propagation (EuCAP)*.

[36] Qifan Pu, Sidhant Gupta, Shyamnath Gollakota, and Shwetak Patel. 2013. Whole-Home Gesture Recognition Using Wireless Signals. In *Proceedings of the 19th annual international conference on Mobile computing and networking (MobiCom)*. 27–38.

[37] Hariharan Rahul, Swarun Suresh Kumar, and Dina Katabi. 2012. Megamimo: Scaling wireless capacity with user demand. In *ACM SIGCOMM Computer Communication Review*, Vol. 4. 1.

[38] WFYT Richards, Yuen Lo, and D Harrison. 1981. An improved theory for microstrip antennas and applications. *IEEE Transactions on antennas and propagation* 29, 1 (1981), 38–46.

[39] Nicolas Scheiner, F. Kraus, Fangyin Wei, Buu Phan, F. Mannan, N. Appenrodt, W. Ritter, J. Dickmann, K. Dietmayer, B. Sick, and Felix Heide. 2020. Seeing Around Street Corners: Non-Line-of-Sight Detection and Tracking In-the-Wild Using Doppler Radar. *IEEE/CVF Conference on Computer Vision and Pattern Recognition (CVPR)* (2020).

[40] D. Steinmetzer, J. Chen, J. Classen, E. Knightly, and M. Hollick. 2015. Eavesdropping with periscopes: Experimental security analysis of highly directional millimeter waves. In *Communications & Network Security*. 335–343.

[41] Sanjib Sur, Teng Wei, and Xinyu Zhang. 2015. Bringing Multi-Antenna Gain to Energy-Constrained Wireless Devices. In *Proceedings of the 14th International Conference on Information Processing in Sensor Networks (IPSN)*. 25–36.

[42] Xin Tan, Zhi Sun, Josep M Jornet, and Dimitris Pados. 2016. Increasing indoor spectrum sharing capacity using smart reflect-array. In *2016 IEEE International Conference on Communications (ICC)*. IEEE, 1–6.

[43] Deepak Vasisht, Anubhav Jain, Chen-Yu Hsu, Zachary Kabelac, and Dina Katabi. 2018. Duet: Estimating user position and identity in smart homes using intermittent and incomplete RF-data. *Proceedings of the ACM on Interactive, Mobile, Wearable and Ubiquitous Technologies (IMWUT)* 2, 2 (2018), 1–21.

[44] Song Wang, Jingqi Huang, Xinyu Zhang, Hyoil Kim, and Sujit Dey. 2020. X-array: Approximating omnidirectional millimeter-wave coverage using an array of phased arrays. In *Proceedings of the 26th Annual International Conference on Mobile Computing and Networking (MobiCom)*. 1–14.

[45] Yan Wang, Jian Liu, Yingying Chen, Marco Gruteser, Jie Yang, and Hongbo Liu. 2014. E-eyes: device-free location-oriented activity identification using fine-grained wifi signatures. In *Proceedings of the 20th annual international conference on Mobile computing and Networking (MobiCom)*. 617–628.

[46] Teng Wei, Shu Wang, Anfu Zhou, and Xinyu Zhang. 2015. Acoustic eavesdropping through wireless vibrometry. In *Proceedings of the 21st Annual International Conference on Mobile Computing and Networking (MobiCom)*. 130–141.

[47] Allen Welkie, Longfei Shangguan, Jeremy Gummeson, Wenjun Hu, and Kyle Jamieson. 2017. Programmable radio environments for smart spaces. In *Proceedings of the 16th ACM Workshop on Hot Topics in Networks*. 36–42.

[48] Qingqing Wu and Rui Zhang. 2019. Towards smart and reconfigurable environment: Intelligent reflecting surface aided wireless network. *IEEE Communications Magazine* 58, 1 (2019), 106–112.

[49] Zhanni Wu, Younes Ra'di, and Anthony Grbic. 2019. Tunable metasurfaces: A polarization rotator design. *Physical Review X* 9, 1 (2019), 011036.

[50] Yaxiong Xie, Yanbo Zhang, Jansen Christian Liando, and Mo Li. 2018. SWAN: Stitched Wi-Fi ANtennas. In *Proceedings of the 24th Annual International Conference on Mobile Computing and Networking (MobiCom)*. 51–66.

[51] Fan Yang, Ruyuan Deng, Shenheng Xu, and Maokun Li. 2018. Design and experiment of a near-zero-thickness high-gain transmit-reflect-array antenna using anisotropic metasurface. *IEEE Transactions on Antennas and Propagation* 66, 6 (2018), 2853–2861.

[52] Qing Yang, Xiaoxiao Li, Hongyi Yao, Ji Fang, Kun Tan, Wenjun Hu, Jiansong Zhang, and Yongguang Zhang. 2013. BigStation: Enabling scalable real-time

signal processingin large MU-MIMO systems. *ACM SIGCOMM Computer Communication Review* 43, 4 (2013), 399–410.

[53] Chia-Yi Yeh and Edward W Knightly. 2018. Feasibility of passive eavesdropping in massive mimo: An experimental approach. In *2018 IEEE Conference on Communications and Network Security (CNS)*. IEEE, 1–9.

[54] Youwei Zeng, Dan Wu, Jie Xiong, Jinyi Liu, Zhaopeng Liu, and Daqing Zhang. 2020. MultiSense: Enabling multi-person respiration sensing with commodity wifi. *Proceedings of the ACM on Interactive, Mobile, Wearable and Ubiquitous Technologies (IMWUT)* 4, 3 (2020), 1–29.

[55] L. Zhang, M. Z. Chen, W. Tang, J. Y. Dai, and T. J. Cui. 2021. A wireless communication scheme based on space- and frequency-division multiplexing using digital metasurfaces. *Nature Electronics* (2021), 1–10.

[56] L. Zhang, X. Q. Chen, S. Liu, Q. Zhang, J. Zhao, J. Y. Dai, G. D. Bai, X. Wan, Q. Cheng, and G. Castaldi. 2018. Space-time-coding digital metasurfaces. *Nature Communications* 9, 1 (2018).

[57] Qianqian Zhang, Ying-Chang Liang, and H Vincent Poor. 2020. Large intelligent surface/antennas (LISA) assisted symbiotic radio for IoT communications. *arXiv preprint arXiv:2002.00340* (2020).

[58] Renjie Zhao, Timothy Woodford, Teng Wei, Kun Qian, and Xinyu Zhang. 2020. M-cube: A millimeter-wave massive MIMO software radio. In *Proceedings of the 26th Annual International Conference on Mobile Computing and Networking (MobiCom)*. 1–14.

[59] Yue Zheng, Yi Zhang, Kun Qian, Guidong Zhang, Yunhao Liu, Chenshu Wu, and Zheng Yang. 2019. Zero-Effort Cross-Domain Gesture Recognition with Wi-Fi.

In *Proceedings of the 17th Annual International Conference on Mobile Systems, Applications, and Services*. ACM, 313–325.

A APPENDIX

Table 1: The parameters of the unit-cell.

Parameter	Value (mm)	Parameter	Value (mm)
L_s	24	W_s	24
L_p	14	W_p	9.8
R	4	t	1.3
L_d	1.3	W_g	1
h_s	3	h_b	0.1
d_v	0.8	d_{bias}	0.4
L_c	13.6	W_c	0.5
W_{bias}	0.2	W_{bg}	0.2